INTERNATIONAL JOURNAL FOR NUMERICAL METHODS IN FLUIDS
Int. J. Numer. Meth. Fluids 2001; **35**: 1–23

A numerical study of turbulent flow over a two-dimensional hill

S. G. Sajjadi[a,*], T. J. Craft[b] and Y. Feng[c]

[a] *CHL, Stennis Space Center, Building 1103, Suite 103, Mississippi 39529, U.S.A.*
[b] *Thermofluid Division, Department of Mechanical Engineering, UMIST, PO Box 88, Manchester, U.K.*
[c] *Centre for Computational Fluid Dynamics and Turbulence, University of Salford, Salford, U.K.*

SUMMARY

Calculations of mean velocities and Reynolds stresses are reported for the recirculating flow established in the wake of two-dimensional polynomial-shaped obstacles that are symmetrical about a vertical axis and mounted in the water channel downstream of a fully developed channel flow for $Re = 6 \times 10^4$. The study involves calculations of mean and fluctuating flow properties in the streamwise and spanwise directions and include comparisons with experimental data [Almeida GP, Durão DFG, Heitor MV. Wake flows behind two-dimensional model hills. *Experimental Thermal and Fluid Science* 1993; **7**: 87–101] for flow around a single obstacle with data resulting from the interaction of consecutive obstacles, using two versions of the low-Reynolds number differential second-moment (DSM) closure model. The results include analysis of the turbulent stresses in local flow co-ordinates and reveal flow structure qualitatively similar to that found in other turbulent flows with a reattachment zone. It is found that the standard isotropization of production model (IPM), based on that proposed by Gibson and Launder [Ground effects on pressure fluctuations in the atmospheric boundary layer. *Journal of Fluid Mechanics* 1978; **86**(3): 191–511], with the incorporation of the wall reflection model of Craft and Launder [New wall-reflection model applied to the turbulent impinging jet. *AIAA Journal* 1992; **32**(12): 2970–2972] predicts the mean velocities quite well, but underestimates the size of the recirculation region and turbulent quantities in the shear layer. These inadequacies are circumvented by adopting a new cubic Reynolds stress closure scheme based on that more recently developed by Craft and Launder [A Reynolds stress closure designed for complex geometries. *International Journal of Heat and Fluid Flow* 1996; **17**: 245–254] which satisfies the two component limit (TCL) of turbulence. In this model the geometry-specific quantities, such as the wall-normal vector or wall distance, are replaced by invariant dimensionless gradient indicators. Also, the model captures the diverse behaviour of the different components of the stress dissipation, ε_{ij}, near the wall and uses a novel decomposition for the fluctuating pressure terms. Copyright © 2001 John Wiley & Sons, Ltd.

KEY WORDS: complex terrain; second-moment closure; turbulent wake flow

---

* Correspondence to: CHL, Stennis Space Center, Building 1103, Suite 103, Mississippi 39529, U.S.A.

Received December 1998
Revised July 1999

1. INTRODUCTION

The study of the turbulent flow over curved surfaces or hills is of great practical importance in engineering and aerodynamics applications, for example, in most types of turbomachinery, flow along guide vanes, and past airfoils. It is also an excellent way of exploring fundamental aspects of air flow over complex terrain for environmental and meteorological problems, such as turbulent transfer and diffusion, which play a critical role in determining the transfer of momentum, heat and moisture in the atmospheric boundary layer. In the case of flow over hills, the effects of shear and turbulence intensity in the approach flow can strongly affect the basic flow structure behind the hills by changing the locations of separation and reattachment on the leeside of a hill. Furthermore, the turbulent flow processes behind rippled sea beds are considered to be responsible for the sediment transport pattern (see Mueller and Gyr [1]).

The changes in turbulent flow over complex terrain may be caused by various mechanisms. For example, in neutrally stable conditions, as in the case of a flow over hills, the flow speeds up over the summit of the hill and slows down in the valley. The changes of mean flow occur because the streamlines are displaced by the hill due to an induced pressure gradient and shear stress perturbation. On the leeside, a separated wake region is formed as a result of a strong adverse pressure gradient established in the leeside of the hill, which changes the flow field not only in the separation region itself but also over the entire hill. The effect of the pressure gradient (due to the blockage effect of the hill) a short distance upstream of the hill forces the boundary layer to undergo a three-dimensional separation. Over steep hills, the boundary layer separates and rolls up downstream of the separation line to form a system of vortices that forms an upstream reverse zone. The vortices are deflected laterally and swept around the base of the hill. Above this zone, the fluid impinges on the hill surface, which can lead to significant concentrations of pollutants when the plume is incident on the hill. The vortex system will produce a high-wall shear stress, and the upstream shear boundary layer could amplify this effect. Near the top of the hill, when the fluid passes over the hill, the strong downflow could form a down-slope wind storm, which may produce damage to human activity, structure, forestry, etc. As above, the upstream shear boundary layer could strongly influence the position and intensity of the down-slope wind storm.

The flow field above the hill can be divided into three regions. Near the surface, in the inner region, the turbulent scales are small enough to be in local equilibrium and adjust to the local velocity gradient, which leads to the three components of normal Reynolds stresses increasing in magnitude. In the intermediate region, above the inner region, the non-linearities and diffusion processes strongly affect the turbulent structure. Well above the surface, in the outer region, the large scales of turbulence are not in local equilibrium, and adjust linearly to the acceleration and curvature of the mean flow as the eddies are advected over the hill. The streamwise curvature has a significant effect on the behaviour of turbulent flow field. The magnitude of this effect is dependent upon the ratio of the shear layer thickness, δ, to the radius of curvature, R, of the hill and is naturally influenced by the ratio R to the height of the hill h.

The dynamics of flow over hills has been considerably investigated in laboratory experiments by Hunt and Snyder [2], Dumas and Fulachier [3], Durão *et al.* [4] and Almeida *et al.* [5], and in field measurements by Deaves [6] and Mason and King [7]. These studies provide useful tests for both theoretical analysis and numerical calculations. The analytical approach, such as rapid distortion theory (RDT) of turbulence, has contributed significantly to understanding dynamics and turbulent structures subjected to high deformation rates (see Sajjadi *et al.* [8]), but this approach is limited to local linearization assumptions for the full non-linear equations, and leads to poor predictions for strong turbulent mixing and diffusion. In view of this, therefore, one is forced to adopt a numerical calculation model, such as a differential second-moment (DSM) closure, which can incorporate all non-linear effects inherent in these flows, in particular the mean acceleration, the estimation of Reynolds stresses and to allow extrapolation to more practical situations to reproduce the flow structure described above with minimum time and effort.

The DSM closure models are developed to suit the above requirements with improving computer technology. One of the earlier and frequently cited of such closure models is the isotropization of production model (IPM) of Launder *et al.* [9], which has been tested over a wide range of flows of practical interest. In this model, a systematic representation for the pressure–strain correlation and turbulent transport terms in derived. Furthermore, the transport equation for the turbulent dissipation rate is derived in conjunction with the Reynolds stress model. Based on this model, series of second-moment closure models have been developed by various authors to improve the earlier proposals, see, for example, Lumley [10], Gibson and Launder [11], Reynolds [12], Fu *et al.* [13] and Lee [14]. All these models are calibrated to suit practical turbulent flows. An important contribution is due to Shih and Lumley [15], who showed that by adding terms quadratic in the Reynolds stresses to the rapid part of pressure strain correlation, ϕ_{ij2}, all the required kinematic constraints can be satisfied, including the exact two-component limit (TCL) as the wall is approached. Shih and Lumley [15] found that reasonable agreement with experimental results could be achieved only by adding selected cubic and quartic products. Fu *et al.* [13] on the other hand, adopted a cubic DSM closure model by retaining the full set of cubic terms, which naturally accommodates the paradoxical effects of (P/ε) on the Reynolds stress field. In this model, as the wall is approached, the stress field does asymptote to a two-dimensional state since, by continuity, velocity fluctuations normal to the wall fall to zero faster than those parallel to it.

Recently there has been renewed interest in developing second-moment closures that are fully realizable and satisfy the TCL of turbulence. In these models it has been tried, as far as possible, to avoid the use of gradient diffusion hypotheses and to represent these processes arising from the interaction between mean flow and turbulent diffusion directly. Furthermore, it has been attempted to make these models applicable in the viscous sublayers by integrating the transport equations right up to the wall itself (see, for example, Craft [16]).

In all DSM closure models of turbulence, the modelling of the pressure–strain term has proved to be formidable task. Usually, following a common practice, the pressure–strain term is decomposed into the linear and non-linear (or return to isotropy and rapid) parts respectively. Many authors obtained analytical expressions for the ‘linear part’ of the pressure–strain rate tensor in terms of the anisotropy of Reynolds stresses, for example, as shown by Lee [14], the coefficients of the seven independent tensor terms are functions of the invariance of the Reynolds stress anisotropy. For near-wall flows, various models have been developed to represent approximately the correct relative levels of the Reynolds stresses in the vicinity of the wall. However, when these schemes are applied to the axisymmetric impinging jet it leads to excessive levels of the turbulent stresses in the vicinity of the stagnation point. This anomalous behaviour of the wall correction near stagnation points has also been recently noted by Murakami *et al.* [17] in a study of a three-dimensional buoyant jet in an enclosure. Thus, Craft and Launder [18] proposed an alternative formulation for the rapid part of the pressure reflection model that gives rise to the aforementioned discrepancies when compared with experiments. For flows over complicated geometries, such as those with strong streamwise curvature or wavy surfaces, employing the pressure reflection terms to account for the damping effects from the wall and surfaces leads to serious errors. This is because the pressure reflection terms usually employ the wall-normal vector or distance in order to determine the direction and account for the damping that is required. However, in complex flow geometries, such a wall-normal distance is often not uniquely defined and, depending on the form adopted, different results are obtained.

A variety of *ad hoc* wall damping functions are currently used that depend on the unit normal to the wall. This feature makes it virtually impossible to reliably apply these models to complex geometries. Consequently, in many applications of second-moment closures to wall-bounded turbulence, the integration is carried out by matching to the law of the wall boundary conditions, which do not formally apply to complex turbulent flows. However, the most disturbing feature here is that many of the commonly used second-moment closures are not even capable of reproducing law-of-the-wall results for an equilibrium turbulent boundary layer unless an *ad hoc* wall reflection term is added. This term typically depends inversely on the distance from the wall, further compromising the ability to apply these models to complex geometries.

Thus, in this paper, following Craft and Launder [19], we apply a low-Reynolds number DSM closure model that does not employ wall distances. Instead, this model relies on turbulence length scale gradients to indicate where there are strong inhomogeneities in the flow. This model has been tested in a number of simple flows, including shear-free walls and surface flows, by Craft and Launder [19] and in more complex geometries by Craft [16]. The aim of this paper is therefore to apply this new model to the flow over a two-dimensional model hill, for which experimental data have been reported by Almeida *et al.* [5], and to compare its performance with a low-Reynolds number version of Gibson and Launder's [11] IPM second-moment closure model.

For the turbulent flow over the two-dimensional model hill considered here, a review may be obtained from an ERCOFTAC Workshop by Bonnin *et al.* [20], in which 38 different numerical calculations, using various turbulence models, were compared with experimental data of Almeida *et al.* [5]. The conclusion was that modifications had to be introduced to the standard high-Reynolds number $k-\varepsilon$ model to obtain a more realistic recirculation region. The compilation of results also showed that resolving the viscosity-affected near-wall layer with either a low-Reynolds number version of the model or with a one-equation model in the viscous sub-layer yielded recirculation lengths that were in fairly good agreement with the experimental data. The results obtained from some non-standard wall functions also showed clearly that the prediction of the separation region depends strongly on the near-wall treatment. However, all models underpredicted the levels of turbulent kinetic energy k and shear stress $\overline{uv}$ in the separation shear layer region.

These underpredictions were also noted by Lien [21], who compared three different turbulence models with the Almeida *et al.* [5] data. The models adopted by Lien [21] were: a linear eddy–viscosity model, non-linear eddy-viscosity models that employ expansions of strain and vorticity components for the Reynolds stresses up to quadratic and cubic products. He concluded that the cubic variant of the non-linear $k-\varepsilon$ model yielded the best results for the separation region, the dip in the wall pressure and peak in the skin friction. Another attempt was also made by Goldberg and Apsley [22], who used a new eddy–viscosity in the low Reynolds $k-\varepsilon$ model and predicted the recirculation flow and mean velocity quite well. Their calculations also underestimated the turbulent shear stress $\overline{uv}$. In this paper we shall also compare our results with those of both Lien [21] and Goldberg and Apsley [22]. We shall also demonstrate that by adopting a turbulence model which is fully realizable and satisfies the TCL of turbulence, better agreement between prediction and experimental data is obtained, particularly for the Reynolds stresses, in both the recirculation and recovery regions.

2. MODELLING APPROACH

2.1. Governing transport equation

Consider an incompressible viscous fluid with the constant density ρ and kinematic viscosity ν, whose mean characteristic velocity is $U_0 = 2.147\ \mathrm{m\,s^{-1}}$, over a two-dimensional model hill. The flow field above the hill may be obtained by solving the following coupled equations, namely the continuity equation, the Reynolds averaged and the Reynolds stress transport equations:

$$\frac{\partial U_i}{\partial x_i} = 0 \tag{2.1}$$

$$\frac{\mathrm{D}U_i}{\mathrm{D}t} = -\frac{1}{\rho}\frac{\partial P}{\partial x_i} + \frac{\partial}{\partial x_j}\left[\nu\left(\frac{\partial U_i}{\partial x_j} + \frac{\partial U_j}{\partial x_i}\right) - \overline{u_i u_j}\right] \tag{2.2}$$

$$\frac{\mathrm{D}\overline{u_i u_j}}{\mathrm{D}t} = P_{ij} + \Pi_{ij} + d_{ij} - \varepsilon_{ij} \tag{2.3}$$

where $x_i = (x, y)$ are the Cartesian co-ordinates, $U_i = (U, V)$ is the time-averaged velocity vector, P is the pressure, $\overline{u_i u_j}$ are the Reynolds stresses and $\mathrm{D}/\mathrm{D}t = (\partial/\partial t) + \boldsymbol{U}\cdot\boldsymbol{\nabla}$. Equation (2.3) is the exact DSM Reynolds stress transport equation, which shows a balance between convection, the production P_{ij}, the pressure correlation Π_{ij}, diffusion d_{ij} and viscous dissipation ε_{ij}. The production term given by

$$P_{ij} = -\left(\overline{u_i u_k}\frac{\partial U_j}{\partial x_k} + \overline{u_j u_k}\frac{\partial U_i}{\partial x_k}\right)$$

is exact and does not require modelling, whilst the diffusion term d_{ij} is given by

$$d_{ij} = \frac{\partial}{\partial x_k}\left(\nu\,\frac{\partial \overline{u_i u_j}}{\partial x_k} - \overline{u_i u_j u_k}\right)$$

The pressure correlation

$$\Pi_{ij} = -\frac{1}{\rho}\left(\overline{u_i\,\frac{\partial p}{\partial x_j}} + \overline{u_j\,\frac{\partial p}{\partial x_i}}\right)$$

is split into a redistributive part ϕ_{ij}, which distributes energy among the components of normal stresses $\overline{u^2}$, $\overline{v^2}$, $\overline{w^2}$, and a pressure diffusion of turbulent kinetic energy, d^p_{ij}, according to

$$\phi_{ij} = \overline{\frac{p}{\rho}\left(\frac{\partial u_i}{\partial x_j} + \frac{\partial u_j}{\partial x_i}\right)} \quad \text{and} \quad d^p_{ij} = -\frac{1}{\rho}\left(\frac{\partial \overline{pu_i}}{\partial x_j} + \frac{\partial \overline{pu_j}}{\partial x_i}\right)$$

In Sections 2.2 and 2.3 different forms of the pressure correlation Π_{ij}, viscous dissipation ε_{ij} and the transport equation governing the dissipation rate ε for the IPM and TCL, which are used in the present investigation, will be introduced respectively.

2.2. IPM model

2.2.1. Pressure strain. The IPM is one of the simplest models for the pressure–strain correlation in the Reynolds stress equations. The correlation ϕ_{ij} is the time-averaged product of the fluctuating pressure and strain rate and it cannot be measured accurately by experiment; although it plays a crucial role in the budget of the Reynolds stress tensor $\overline{u_i u_j}$. There are two contributions to this process, one associated with a non-linear interaction, ϕ_{ij1}, which is the turbulence–turbulence interaction process, and the other, ϕ_{ij2}, involving a linear or rapid mean velocity–turbulence interaction process. The models for these processes adopted here based on the original proposal of Rotta [23] are

$$\phi_{ij1} = -c_1\,\frac{\varepsilon}{k}\left(\overline{u_i u_j} - \frac{1}{3}\,\delta_{ij}\overline{u_k u_k}\right) \quad \text{and} \quad \phi_{ij2} = -c_2\left(P_{ij} - \frac{1}{3}\,\delta_{ij}P_{kk}\right) \tag{2.4}$$

where $k = (u^2 + v^2 + w^2)^{1/2}$ is the turbulent kinetic energy.

In a simple shear flow, ϕ_{ij2} acts to diminish the effective generation of $\overline{u^2}$ by redistributing it equally to the normal stresses in the x_2- and x_3-directions. The effect of ϕ_{ij2} is to oppose this redistribution and hence to reduce the energy flow rate to $\overline{v^2}$.

However, this model has two weaknesses. From experimental data it has been shown that increasing (P/ε) appreciably altered the orientation of the principal axes of stress field relative to those of the strain field. Secondly, the model cannot satisfy the exact two-dimensional limit as the wall is approached: $\phi_{\alpha\alpha 2} = 0$ if $u_\alpha = 0$ (Lumley [10]), where u_α is the fluctuating velocity in direction x_α. This problem has been circumvented by Shih and Lumley [15] who added selected cubic and quartic products to ϕ_{ij2} in the Reynolds stress, so that all the required kinematic constraints can be satisfied, including the exact two-dimensional limit as the wall is approached.

2.2.2. Near-wall modifications for pressure–strain term. The presence of a rigid boundary necessitates a correction to these processes in order to reduce the intensity of velocity fluctuations normal to the wall in the vicinity of a surface. Gibson and Launder [11] adopted the following form:

$$\phi^{w}_{ij1} = c'_1 \frac{\varepsilon}{k}\left(\overline{u_l u_m}\, n_l n_m \delta_{ij} - \frac{3}{2}\overline{u_i u_l}\, n_j n_l - \frac{3}{2}\overline{u_j u_l}\, n_i n_l\right) f\left(\frac{L}{c_l y}\right) \tag{2.5}$$

$$\phi^{w}_{ij2} = c'_2\left(\phi_{lm2} n_l n_m \delta_{ij} - \frac{3}{2}\phi_{il2} n_j n_l - \frac{3}{2}\phi_{jl2} n_i n_l\right) f\left(\frac{L}{c_l y}\right) \tag{2.6}$$

Here n_k are unit vectors normal to the wall, L is the length scale given by $L = k^{3/2}/\varepsilon$ and f is the wall proximity function.

The form of ϕ^{w}_{ij1}, given by Equation (2.5), always ensures that the correction to ϕ_{ij1} acts as a sink in that budget for the component of normal Reynolds stress perpendicular to the wall and as a source in the other two components of normal Reynolds stresses. The action of ϕ^{w}_{ij2}, however, depends on the nature of the mean strain field.

More recently, Craft and Launder [18] considered a new form of ϕ^{w}_{ij2} that involves linear products of the velocity gradient and Reynolds stress tensors. The form adopted by them may be expressed as

$$\begin{aligned}\phi^{w}_{ij2} = {} & -0.08\frac{\partial U_l}{\partial x_m}\overline{u_l u_m}(\delta_{ij} - 3n_i n_j) f\left(\frac{L}{c_l y}\right) + 0.4k\frac{\partial U_l}{\partial x_m} n_l n_m\left(n_i n_j - \frac{1}{3}\delta_{ij}\right) f\left(\frac{L}{c_l y}\right) \\ & - 0.1k a_{lm}\left(\frac{\partial U_k}{\partial x_m} n_l n_k \delta_{ij} - \frac{3}{2}\frac{\partial U_i}{\partial x_m} n_l n_j - \frac{3}{2}\frac{\partial U_j}{\partial x_m} n_l n_i\right) f\left(\frac{L}{c_l y}\right)\end{aligned} \tag{2.7}$$

where

$$a_{ij} \equiv \frac{\left(\overline{u_i u_j} - \frac{1}{3}\delta_{ij}\overline{u_k u_k}\right)}{k} \tag{2.8}$$

In a simple shear flow, only the first of the three terms in Equation (2.7) affects the normal stresses; a fraction of the turbulent kinetic energy generation is 'redistributed' from the component normal to the wall to the other components. Here, we use Equation (2.7) in order to overcome the strong inhomogeneities in the near-wall region.[1]

---

[1] This was illustrated by Sajjadi and Aldridge [30] for flow over asymmetrical bed forms.

2.2.3. Triple correlations. In the present work, the triple correlations are approximated by the Hanjalic and Launder [24] proposal

$$\overline{u_i u_j u_k} = -c_s \frac{k}{\varepsilon}\left[\overline{u_i u_l}\frac{\partial \overline{u_j u_k}}{\partial x_l} + \overline{u_j u_l}\frac{\partial \overline{u_i u_k}}{\partial x_l} + \overline{u_k u_l}\frac{\partial \overline{u_j u_i}}{\partial x_l}\right]$$

2.2.4. Dissipation rate equation. The viscous dissipation tensor, ε_{ij}, is modelled by

$$\varepsilon_{ij} = \left\{\frac{2}{3}\,\delta_{ij}(1-f_s) + \frac{f_s F}{k}\,(\overline{u_i u_j} + \overline{u_i u_k} n_k n_j + \overline{u_j u_k} n_k n_i + \overline{u_k u_\ell} n_k n_\ell \delta_{ij})\right\}\varepsilon \tag{2.9}$$

with

$$f_s = \mathrm{e}^{-Re_\mathrm{t}/40}$$

where $Re_\mathrm{t} = k^2/\nu\varepsilon$ is the turbulent Reynolds number and

$$F = \left(1 + \frac{5}{2}\frac{\overline{u_p u_q} n_p n_q}{k}\right)^{-1}$$

The scalar ε is obtained by solving the following transport equation:

$$\frac{\mathrm{D}\varepsilon}{\mathrm{D}t} = \frac{\varepsilon}{2k}\,(c_{\varepsilon 1} + 2)P_{kk} - c_{\varepsilon 2}\frac{\varepsilon\tilde{\varepsilon}}{k} + c_{\varepsilon 3}\,\nu\frac{k}{\varepsilon}\,\overline{u_j u_k}\left(\frac{\partial^2 U_i}{\partial x_j\,\partial x_\ell}\right)\left(\frac{\partial^2 U_i}{\partial x_k\,\partial x_\ell}\right) + \frac{\partial}{\partial x_k}\left(c_\varepsilon \frac{k}{\varepsilon}\,\overline{u_k u_\ell}\,\frac{\partial \varepsilon}{\partial x_\ell}\right) \tag{2.10}$$

where

$$\tilde{\varepsilon} = \varepsilon - 2\nu\left(\frac{\partial\sqrt{k}}{\partial x_\ell}\right)^2$$

is a quantity that vanishes at the wall.

The IPM model coefficients are tabulated in Table I.

2.3. TCL model

The model adopted here is based on that originally proposed by Craft and Launder [19].

Table I. The coefficients used in IPM model.

c_1	c_2	c_1'	c_2'	c_l	c_ε	$c_{\varepsilon 1}$	$c_{\varepsilon 2}$	$c_{\varepsilon 3}$	c_s
1.8	0.6	0.5	0.3	2.44	0.15	$1.45(1-f_s)+2f_s$	1.92	0.3	0.11

2.3.1. Length scale gradient. The present model adopts two inhomogeneous indicators based on gradients of the turbulent length scale $L \equiv k^{3/2}/\varepsilon$. The parameter

$$N_i \equiv \frac{\partial L}{\partial x_i}$$

has been used by some authors, see, for example, Launder and Tselepidakis [25]. For the present purpose it is desirable to normalize N_i so that it flags regions of strong inhomogeneity rather than the magnitude of the length-scale gradient itself. This is achieved by defining d_i as

$$d_i \equiv \frac{N_i}{[a + (N_k N_k)^{1/2}]}$$

where the coefficient $a = 0.5$ and $(N_k N_k)^{1/2}$ is typically about 2.5 in an equilibrium near-wall turbulent region.

In the buffer region of wall shear flow, the length scale levels out, giving undesirably small levels of d_i where there is a highly inhomogeneous region. The problem is circumvented by introducing flatness factor A (see Lumley [10]) so that

$$N_i^A \equiv \frac{\partial}{\partial x_i}(LA) \quad \text{and} \quad d_i^A = \frac{N_i^A}{a + (N_k^A N_k^A)^{1/2}}$$

A becomes unity in isotropic turbulence and vanishes at a wall, where the turbulent fluctuations reduce to a TCL.

2.3.2. Pressure correlation. In near-wall flows the pressure correlation includes two terms, the pressure strain, denoted by ϕ_{ij}, and pressure diffusion, d_{ij}^p, which is equal to zero in homogeneous flows. In this model the decomposition of Π_{ij} is written as

$$\Pi_{ij} = \phi_{ij}^* + \frac{\overline{u_i u_j}}{2k} d_{kk}^p$$

and ϕ_{ij}^* is modelled as

$$\phi_{ij}^* = \phi_{ij1}^* + \phi_{ij2}^* + \phi_{ij1}^{inh} + \phi_{ij2}^{inh}$$

where

$$\phi_{ij1}^* = -c_1\tilde{\varepsilon}\left[a_{ij} + c_1'\left(a_{ik}a_{kj} - \frac{1}{3}A_2\delta_{ij}\right)\right] - \tilde{\varepsilon}Aa_{ij} \tag{2.11}$$

$$
\begin{aligned}
\phi^{*}_{ij2} = &-0.6\left(P_{ij} - \frac{2}{3}\,\delta_{ij}P_{kk}\right) + 0.6a_{ij}P_{kk} \\
&-0.2\left[\frac{\overline{u_l u_i}\,\overline{u_k u_j}}{k}\left(\frac{\partial U_k}{\partial x_l} + \frac{\partial U_l}{\partial x_k}\right) - \frac{\overline{u_l u_k}}{k}\left(\overline{u_i u_k}\,\frac{\partial U_j}{\partial x_l} + \overline{u_j u_k}\,\frac{\partial U_i}{\partial x_l}\right)\right] \\
&-c_2[A_2(P_{ij} - D_{ij}) + 3a_{mi}a_{nj}(P_{mn} - D_{mn})] + c'_2 \\
&\times\left\{\left(\frac{7}{15} - \frac{A_2}{4}\right)\left(P_{ij} - \frac{1}{3}\,\delta_{ij}P_{kk}\right) + 0.2\left[a_{ij} - \frac{1}{2}\left(a_{ik}a_{kj} - \frac{1}{3}\,\delta_{ij}A_2\right)\right]P_{kk} - 0.05a_{ij}a_{lk}P_{kl}\right. \\
&+0.1\left[\frac{\overline{u_i u_m}}{k}\,P_{mj} + \frac{\overline{u_j u_m}}{k}\,P_{mi} - \frac{2}{3}\,\delta_{ij}\,\frac{\overline{u_l u_m}}{k}\,P_{ml}\right] \\
&\left.+0.1\left[\frac{\overline{u_l u_i}\,\overline{u_k u_j}}{k^2} - \frac{1}{3}\,\delta_{ij}\,\frac{\overline{u_l u_m}\,\overline{u_k u_m}}{k^2}\right]\left[6D_{lk} + 13k\left(\frac{\partial U_l}{\partial x_k} + \frac{\partial U_k}{\partial x_l}\right)\right] + 0.2\,\frac{\overline{u_l u_i}\,\overline{u_k u_j}}{k^2}\,(D_{lk} - P_{lk})\right\}
\end{aligned}
\tag{2.12}
$$

$$
\begin{aligned}
\phi^{inh}_{ij1} = &f_{w1}\,\frac{\varepsilon}{k}\left(\overline{u_l u_k}d_l d_k\delta_{ij} - \frac{3}{2}\,\overline{u_i u_k}d_j d_k - \frac{3}{2}\,\overline{u_j u_k}d_i d_k\right) \\
&+f'_{w1}\,\frac{k^2}{\varepsilon}\left(\overline{u_k u_l}\,\frac{\partial\sqrt{A}}{\partial x_k}\,\frac{\partial\sqrt{A}}{\partial x_l}\,\delta_{ij} - \frac{3}{2}\,\overline{u_i u_k}\,\frac{\partial\sqrt{A}}{\partial x_k}\,\frac{\partial\sqrt{A}}{\partial x_j} - \frac{3}{2}\,\overline{u_j u_k}\,\frac{\partial\sqrt{A}}{\partial x_k}\,\frac{\partial\sqrt{A}}{\partial x_i}\right) \\
&\times f''_{w1}\,\frac{\varepsilon}{k^2}\left[\overline{u_l u_k}\;\overline{u_k u_n}d_n d_l\delta_{ij} - \frac{3}{2}\,\overline{u_i u_k}\;\overline{u_k u_n}d_n d_j - \frac{3}{2}\,\overline{u_j u_k}\;\overline{u_k u_n}d_n d_i\right]
\end{aligned}
\tag{2.13}
$$

$$
\phi^{inh}_{ij2} = f_{w2}k\,\frac{\partial U_l}{\partial x_n}\,d_l d_n\left(d_i d_j - \frac{1}{3}\,d_k d_k\delta_{ij}\right)
\tag{2.14}
$$

and

$$
D_{ij} = -\left(\overline{u_i u_k}\,\frac{\partial U_k}{\partial x_j} + \overline{u_j u_k}\,\frac{\partial U_k}{\partial x_i}\right)
$$

$$
\tilde{\varepsilon} = \varepsilon - 2v\left(\frac{\partial\sqrt{k}}{\partial x_j}\right)^2 - \frac{1}{2}f_h\varepsilon^{*}_{kk}
$$

$c_1 = 3.1f_A f_{Re_{\mathrm{t}}}\min(A_2^{1/2}, 0.5^{1/2})$, $c'_1 = 1.1$, $c_2 = \min(0.55, A^{1.5})$, $c'_2 = \min(0.6, A^{1.5})$, $f_{w1} = 2\,\mathrm{e}^{-0.0018Re_{\mathrm{t}}^2}/(0.0005 + \mathrm{e}^{-0.0018Re_{\mathrm{t}}^2})$, $f'_{w1} = 0.22$, $f_{w2} = 5f_A$, $f''_{w1} = 0.8A_2f'_{Re_{\mathrm{t}}} + 0.1$, $f_{Re_{\mathrm{t}}} = \min(Re_{\mathrm{t}}/160, 1)$, $f'_{Re_{\mathrm{t}}} = \min[1, \max(0.1 - (Re_{\mathrm{t}} - 50)/85)]$,

$$
f_A = \begin{cases} (A/14)^{1/2} & A < 0.05 \\ (A/0.7)^{1/2} & 0.05 < A < 0.7 \\ A^{1/2} & A > 0.7 \end{cases}
\tag{2.15}
$$

In Equation (2.11), A_2 and A are the invariants of the Reynolds stress anisotropy tensor defined as $A_2 = a_{ij}a_{ij}$, $A = 1 - 9/8(A_2 - A_3)$, where $A_3 = a_{ij}a_{jk}a_{ki}$ and a_{ij} is defined by Equation (2.8).

The term ϕ_{ij1}^{inh} can be interpreted as being an inhomogeneous correction to ϕ_{ij1}^* because it involves the length-scale gradient term d_i. The ϕ_{ij2}^{inh} correction to the mean strain-dependent part has a significant effect only in an impinging flow.

The pressure diffusion term adopts the following form:

$$\overline{pu_k}/\rho = -(0.5d_k + 1.1d_k^A)(\nu\varepsilon k A A_2)^{1/2}[c_{pd1}A_2 + c_{pd2}Re_{\mathrm{t}}^{-1/4}\exp(-Re_{\mathrm{t}}/40)]$$

where

$$c_{pd1} = 1.0 + 2.0\exp(-Re_{\mathrm{t}}/40), \qquad c_{pd2} = 0.4$$

2.3.3. Dissipation tensor. The present work employs the following composite form specifically to address the behaviour of ε_{ij} near a wall as indicated by the direct numerical simulation (DNS) data of Kim *et al.* [26]:

$$\varepsilon_{ij} = \left(1 - f_h \frac{\varepsilon_{kk}^*}{2\varepsilon}\right)\left[(1 - f_\varepsilon)(\varepsilon'_{ij} + \varepsilon''_{ij})/D + \frac{2}{3}f_\varepsilon \varepsilon \delta_{ij}\right] + f_h \varepsilon_{ij}^* \tag{2.16}$$

where

$$\varepsilon'_{ij} = \varepsilon\frac{\overline{u_iu_j}}{k} + 2\nu\frac{\overline{u_lu_n}}{k}\frac{\partial\sqrt{k}}{\partial x_l}\frac{\partial\sqrt{k}}{\partial x_n}\delta_{ij} + 2\nu\frac{\overline{u_lu_i}}{k}\frac{\partial\sqrt{k}}{\partial x_j}\frac{\partial\sqrt{k}}{\partial x_l}\delta_{ij} + 2\nu\frac{\overline{u_lu_j}}{k}\frac{\partial\sqrt{k}}{\partial x_i}\frac{\partial\sqrt{k}}{\partial x_l}\delta_{ij}$$

$$\varepsilon''_{ij} = \varepsilon\left[2\frac{\overline{u_lu_k}}{k}d_l^Ad_k^A\delta_{ij} - \frac{\overline{u_lu_i}}{k}d_l^Ad_j^A - \frac{\overline{u_lu_j}}{k}d_l^Ad_i^A\right]f_R$$

$$\varepsilon_{ij}^* = 0.2\nu\left(\frac{\partial\sqrt{kA}}{\partial x_k}\frac{\partial\sqrt{kA}}{\partial x_k}\delta_{ij} + 2\frac{\partial\sqrt{kA}}{\partial x_i}\frac{\partial\sqrt{kA}}{\partial x_j}\right)$$

and

$$D = \frac{\varepsilon'_{kk} + \varepsilon''_{kk}}{2\varepsilon}$$

$$f_R = (1 - A)\min\left[\left(\frac{Re_{\mathrm{t}}}{80}\right)^2, 1.0\right], \qquad f_\varepsilon = A^{1/2}, \qquad f_h = 1 - \exp\left(-\frac{Re_{\mathrm{t}}}{50}\right)$$

The gradient terms of ε'_{ij} are only effective across the viscous sub-layer where k gradients are steep. The term ε''_{ij} principally has the effect of producing the dip in ε_{12} in the near-wall DNS studies. The term ε_{ij}^* is designed to improve the behaviour of ε_{ij} at a free surface where there are significant inhomogeneous effects and the turbulent Reynolds number is large.

2.3.4. Triple correlations. In contrast to the IPM model, the triple correlations for the TCL model are obtained from an algebraic simplification of their transport equations, which may be cast as

$$\frac{\mathrm{D}\overline{u_i u_j u_k}}{\mathrm{D}t} = P^1_{ijk} + P^2_{ijk} + \phi_{ijk} + d_{ijk} - \varepsilon_{ijk} \tag{2.17}$$

where the production terms

$$P^1_{ijk} = \overline{u_i u_j}\,\frac{\partial \overline{u_k u_l}}{\partial x_l} + \overline{u_i u_k}\,\frac{\partial \overline{u_j u_l}}{\partial x_l} + \overline{u_k u_j}\,\frac{\partial \overline{u_i u_l}}{\partial x_l}$$

$$P^2_{ijk} = -\,\overline{u_i u_j u_l}\,\frac{\partial U_k}{\partial x_l} - \overline{u_i u_k u_l}\,\frac{\partial U_j}{\partial x_l} + \overline{u_k u_j u_l}\,\frac{\partial U_i}{\partial x_l}$$

are exact. Invoking the Millionshtchikov [27] hypothesis for the fourth-order moments appearing in the diffusion term d_{ijk} leads to

$$d_{ijk} = -\frac{\partial}{\partial x_l}\,(\overline{u_i u_j}\;\overline{u_k u_l} + \overline{u_i u_k}\;\overline{u_j u_l} + \overline{u_k u_j}\;\overline{u_i u_l})$$

whilst ε_{ijk} is modelled as $-2\varepsilon\overline{u_i u_j u_k}/k$. The pressure correlation ϕ_{ijk} is modelled as

$$\phi_{ijk} = \phi_{ijk1} + \phi_{ijk2} + \phi^{inh}_{ijk}$$

where

$$\phi_{ijk1} = -\,c_{t1}\,\frac{\varepsilon}{k}\,\overline{u_i u_j u_k}$$

$$\phi_{ijk2} = -\,c_{t2}P^2_{ijk} + c'_{2t}\left(\overline{u_i u_j u_k}\,\frac{\partial U_l}{\partial x_k} + \overline{u_i u_k u_l}\,\frac{\partial U_l}{\partial x_j} + \overline{u_k u_j u_l}\,\frac{\partial U_l}{\partial x_i}\right)$$

$$\phi^{inh}_{ijk} = c_{tw}\left(\frac{\partial \overline{u_i u_n}}{\partial x_r}\,\delta_{jk} + \frac{\partial \overline{u_j u_n}}{\partial x_r}\,\delta_{ik} + \frac{\partial \overline{u_r u_n}}{\partial x_r}\,\delta_{ji}\right)\overline{u_l u_r}\,d^A_l d^A_n$$

represent a return to isotropy term, a mean strain-dependent term and an inhomogeneity related term respectively, and the coefficients are taken as

$$c_{t1} = 4.2, \quad c_{t2} = 1.0, \quad c'_{t2} = 0.2A, \quad c_{tw} = 0.5$$

Following Craft [16], the coefficient c_{t2} is taken as unity since inclusion of the P^2_{ijk} term tends to cause numerical instabilities in the code. The other coefficients are tuned to give good agreement with available boundary layer data. The triple moments are then obtained by

Table II. The coefficients used in TCL model.

$c_{\varepsilon 1}$	$c_{\varepsilon 2}$	A_d	$c'_{\varepsilon 2}$	$c_{\varepsilon 3}$	$c_{\varepsilon 4}$	$c_{\varepsilon 5}$	c_ε	c_s	c'_s
1.0	$\dfrac{1.92}{1+0.7A_d\sqrt{A_2}}$	max(0.2, A)	1.0	1.55	1.0	1.0	0.09	1.0	0.11

neglecting the left-hand side of Equation (2.17), and solving the resultant algebraic relations for $\overline{u_iu_ju_k}$.

2.3.5. Dissipation rate equation. The dissipation rate $\tilde{\varepsilon}$ is obtained from the transport equation

$$\frac{\mathrm{D}\tilde{\varepsilon}}{\mathrm{D}t} = c_{\varepsilon 1}\frac{\tilde{\varepsilon}P_{kk}}{2k} - c_{\varepsilon 2}\frac{\tilde{\varepsilon}^2}{k} - c'_{\varepsilon 2}\frac{(\varepsilon - \tilde{\varepsilon})\tilde{\varepsilon}}{k} + \frac{\partial}{\partial x_l}\left[\left(\nu\delta_{lk} + c_\varepsilon\overline{u_lu_k}\frac{k}{\varepsilon}\right)\frac{\partial\tilde{\varepsilon}}{\partial x_k}\right] + c_{\varepsilon 3}\nu\overline{u_iu_j}\frac{k}{\varepsilon}\frac{\partial^2 U_k}{\partial x_i x_l}$$
$$+ c_{\varepsilon 4}\nu\frac{\overline{u_iu_j}}{\varepsilon}\frac{\partial k}{\partial x_i}\frac{\partial U_l}{\partial x_k}\frac{\partial^2 U_l}{\partial x_k x_j} + c_{\varepsilon 5}A^{1/2}(1 - A)\frac{\varepsilon}{\sqrt{k}}\overline{u_iu_j}\frac{\partial A}{\partial x_i}\frac{\partial}{\partial x_j}\left(\frac{k^{3/2}A^{1/2}}{\varepsilon}\right) \qquad (2.18)$$

These TCL model coefficients are given in Table II.

3. NUMERICAL SCHEME

The numerical scheme adopted here is based on the fully conservative, structured finite volume method within which the volumes are non-orthogonal and collocated such that all flow variables are stored at one and the same set of notes. To ease the task of discretization and to enhance the conservative property of the scheme, a Cartesian decomposition of the velocity field is used. The solution algorithm is iterative in nature, approaching the steady solutions with the aid of a pressure–correction scheme.

As mentioned in the above paragraph, the discretization process is preceded by a transformation of the Cartesian co-ordinates of the governing equations to the non-orthogonal co-ordinates ξ and η using the Jacobian transformation matrix. Thus, the transport equation for any scalar property Φ may be expressed in non-orthogonal direction as

$$\frac{\partial}{\partial\xi}\left(\rho U^{(\xi,\eta)}\Phi - J^{-1}\alpha_\Phi\frac{\partial\Phi}{\partial\xi}\right) + \frac{\partial}{\partial\eta}\left(\rho V^{(\xi,\eta)}\Phi - J^{-1}\beta_\Phi\frac{\partial\Phi}{\partial\eta}\right) = JS_\Phi \qquad (3.1)$$

where $U^{(\xi,\eta)} = Uy_\eta - Vx_\eta$ and $V^{(\xi,\eta)} = Vx_\xi - Uy_\xi$ are contravariant velocity components, J is the Jacobian of the transformation, S_Φ is the source terms including diffusive terms, pressure terms in the momentum equation and $\alpha_\Phi = \Gamma_\Phi(y_\eta^2 + x_\eta^2)$ and $\beta_\Phi = \Gamma_\Phi(y_\xi^2 + x_\xi^2)$, where Γ_Φ is isotropic diffusivity and the subscripts ξ and η denote partial differentiations.

Equation (3.1) is integrated over the volume to yield a balance of face fluxes and volume-integrated net source

$$
\begin{aligned}
&(\rho U^{(\xi,\eta)})_{\mathrm{E}}\Phi_{\mathrm{E}} - (\rho U^{(\xi,\eta)})_{\mathrm{W}}\Phi_{\mathrm{W}} + (\rho V^{(\xi,\eta)})_{\mathrm{N}}\Phi_{\mathrm{N}} - (\rho U^{(\xi,\eta)})_{\mathrm{S}}\Phi_{\mathrm{S}}\\
&\quad = JS_{\Phi} + [(\alpha_{\Phi}J^{-1})_{\mathrm{E}} + (\alpha_{\Phi}J^{-1})_{\mathrm{W}} + (\beta_{\Phi}J^{-1})_{\mathrm{N}} + (\beta_{\Phi}J^{-1})_{\mathrm{S}}]\Phi_{P}\\
&\qquad - [(\alpha_{\Phi}J^{-1})_{\mathrm{E}}\Phi_{\mathrm{E}} + (\alpha_{\Phi}J^{-1})_{\mathrm{W}}\Phi_{\mathrm{W}} + (\beta_{\Phi}J^{-1})_{\mathrm{N}}\Phi_{\mathrm{N}} + (\beta_{\Phi}J^{-1})_{\mathrm{S}}\Phi_{\mathrm{S}}]
\end{aligned}
$$

The convection fluxes for the momentum equations are approximated with a higher-order upstream scheme QUICK of Leonard [28], and for the turbulent transport equation by a total variation diminishing (TVD)-type MUCL scheme of van Leer [29]. The latter is applied to the transport equations governing turbulence properties because the QUICK scheme has a tendency to provoke oscillations in regions of steep property variations. With these approximations, together with appropriate expressions for diffusive fluxes, cast in the finite volume integrated form (2.2) and (2.3), a weighted-average equation may be obtained of the form

$$A_P\Phi_P = \sum_i A_i\Phi_i + JS_{\Phi}, \quad i = \mathrm{E, W, N, S}$$

where Φ represents any of the momentum or any of the scalar transport components with corresponding sources S_{Φ}, while $A_P = \Sigma_i A_i$ and the A coefficients contain convective and diffusive contributions linking neighbouring nodes to P. For more details the reader is referred to the work of Sajjadi and Aldridge [30] and Sajjadi and Waywell [31].

The numerical scheme adopted in this study converged after 750 iterations for the IPM model and 1200 for the TCL model. The typical CPU time per iteration was about 4 s for the IPM model and about 6 s for the TCL model. The numerical scheme is very robust and no major difficulty was ever encountered.

The shape of the hill is the inverse of a fourth-order polynomial. More detail description can be found in Almeida *et al.* [5]. A grid refinement exercise was carried out over the computational domain, of physical dimensions $x(-100–500\ \mathrm{mm})$ and $y(0–170\ \mathrm{mm})$, and Figure 1 shows the final 120 × 120 grid that was found to give grid-independent results. As can be seen, a large number of nodes are concentrated in the near-wall regions in order to capture the steep gradients found.

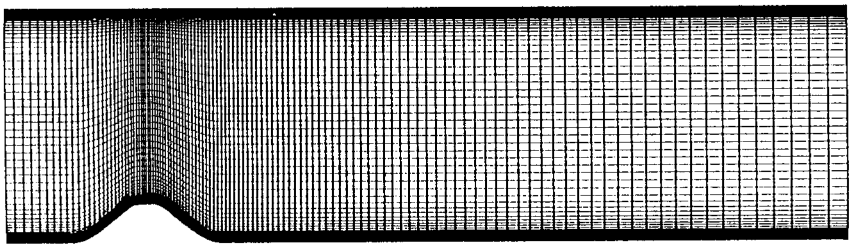

Figure 1. Computational grid.

3.1. Initial and boundary conditions

The inlet condition for mean velocity U, V, Reynolds stresses $\overline{u^2}$, $\overline{v^2}$, $\overline{uv}$, the turbulent kinematic energy and the dissipation rate were obtained by solving a separate one-dimensional calculation of a fully developed channel flow.

At the outflow plane, we set

$$V = \frac{\partial U}{\partial x} = \frac{\partial k}{\partial x} = \frac{\partial \varepsilon}{\partial x} = \frac{\partial \overline{u^2}}{\partial x} = \frac{\partial \overline{v^2}}{\partial x} = \frac{\partial \overline{uv}}{\partial x} = 0$$

The boundary condition at the top and bottom surfaces are the no-slip condition on the velocity and Reynolds stress components, whilst for the dissipation equation we set

$$\varepsilon = 2\nu\left(\frac{\partial\sqrt{k}}{\partial x_j}\right)^2$$

4. RESULTS AND COMPARISON

4.1. Comparison with the experiment

In this section we present detailed investigation of the flow over the two-dimensional model hill mounted in the water channel at $Re = 6 \times 10^4$. The results of computations for both the IPM and TCL low-Reynolds number DSM models will be compared with the laboratory experiment of Almeida *et al.* [5].

The comparison of the mean streamwise velocity profile U, predicted with both the IPM and TCL models, with experimental data at various x locations along the channel is shown in Figure 2.[2] As can be seen from this figure, a considerably thin boundary layer along the upstream surface of the hill is formed near the reattachment point, which accelerates strongly as it approaches the top of the hill. The deflection of the flow by the hill is associated with the

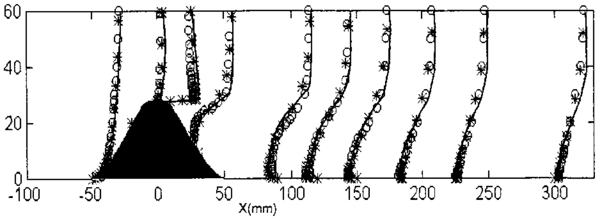

Figure 2. Mean velocity profiles U at various x stations; —, TCL model; $* * *$, IPM model; ○, experimental data of Almeida *et al.* [5].

---

[2] Note that in this paper all profiles for the mean and turbulent stresses are plotted on every fourth grid point.

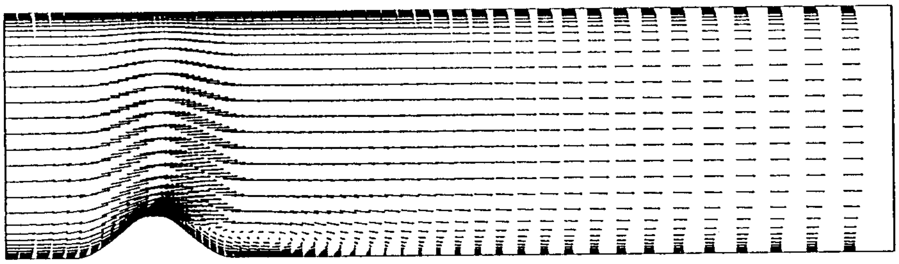

Figure 3. Mean velocity vectors for TCL model.

maximum values of the mean streamwise velocity above the hill of $U/U_0 = 1.08$ at $y/h = 1.003$ for the IPM model and $U/U_0 = 1.21$ at $y/h = 1.028$ for the TCL model. They correspond approximately to the laboratory experiment value of $U/U_0 = 1.27$ at $y/h = 1.036$. Therefore, both models provide a good prediction for the mean streamwise velocity. On the whole, both models capture the main flow features and agree well with the experimental data.

It is now interesting to consider the evolution of the separated shear layer emerging from the top of the hill. Figure 3 shows the predicted velocity vectors for the flow over the hill using the TCL Reynolds stress model. As can be seen from this diagram there is a recirculation region behind the hill and the flow reattaches at $x/h = 4.82$, which is slightly higher than the experimental value of $x/h = 4.5$. In contrast, the IPM model predicts an earlier reattachment at $x/h = 3.9$. This figure also shows that the wall boundary layer formed at the rising surface of the hill remains quite thin up to the downstream crest. Then it spreads as the separation point is approached, where it becomes a free shear layer detached from the surface in a way qualitatively similar to that reported by Buckles *et al.* [32].

In Figures 4 and 5 the normal stresses $\overline{u^2}$ and $\overline{v^2}$ predicted by both the IPM and TCL models, are compared with experimental data. These results show a region of high-velocity fluctuations along the shear layer downstream of the hill in a way similar to that found in the laboratory experiment. Peak values of normal stresses occur in the zones characterized by the highest mean velocity gradients. The turbulent flow is anisotropic, with values of $\overline{u^2}$

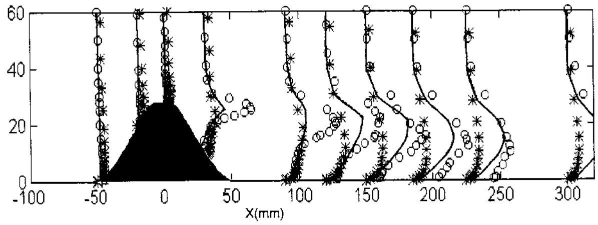

Figure 4. Turbulent normal stress profiles $\overline{u^2}$ at various x stations; —, TCL model; $* * *$, IPM model; ○, experimental data of Almeida *et al.* [5].

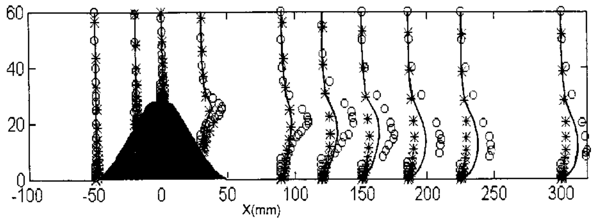

Figure 5. Turbulent normal stress profiles $\overline{v^2}$ at various x stations; —, TCL model; $***$, IPM model; ○, experimental data of Almeida *et al.* [5].

consistently higher than those of $\overline{v^2}$, with the exception of the separation zone. In the free stream, the levels of turbulence anisotropy reach those of the undisturbed flow, with vertical velocity fluctuations half of that in the longitudinal direction. As can be seen from these figures, the IPM model underpredicts the turbulent velocities for both $\overline{u^2}$ and $\overline{v^2}$. In contrast, the TCL model provides a better prediction for both of these components of Reynolds stresses. It is worth noting that the TCL model also provides a much better recovery rate for both components of the normal stresses beyond the distance of $x = 200$ mm downstream of the hill.

The distribution of the turbulent shear stress $\overline{uv}$ is shown in Figure 6, which quantifies the turbulent diffusion along the shear layer and is consistent with the direction of the mean flow. The maximum values occur along the direction of the normal stresses and are larger than those found downstream of a three-dimensional surface mounted hill [4]. As can be seen, the turbulent shear stress is underpredicted in the recirculation region. It is probably this underprediction that results in the overprediction of the reciruclation strength. Further downstream, at around $x = 130$ mm, this underprediction becomes less and a better agreement between the TCL model and the experimental data is obtained. At $x = 150$ mm and beyond a very good agreement between the TCL model and the experiment is obtained. Note, incidentally, that up to $x = 200$ mm the IPM model still underpredicts the peak shear stress close to the wall.

Figure 7 shows the distribution of the turbulent kinetic energy k, in which the experimental data is based on $k = 0.5(\overline{u^2} + 2\overline{v^2})$ since no experimental data is available for the turbulent

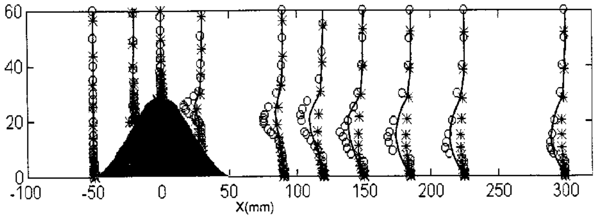

Figure 6. Turbulent normal stress profiles $\overline{uv}$ at various x stations; —, TCL model; $***$, IPM model; ○, experimental data of Almeida *et al.* [5].

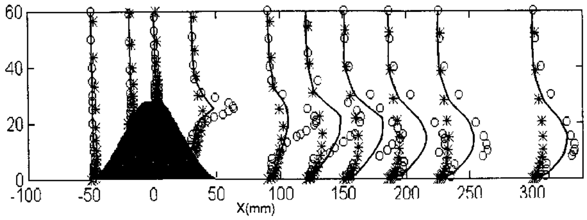

Figure 7. Turbulent normal stress profiles k at various x stations; —, TCL model; $* * *$, IPM model; ○, experimental data of Almeida *et al.* [5].

normal stress $\overline{w^2}$. As can be seen from this figure, the turbulent kinetic energy increases with the distance from the top of the hill up to the reattachment point and then decreases significantly due to the upward tilting of the flow at the upstream face of the hill. This is because downstream of the top of the hill, the overall effect of positive shear strains is to increase turbulent intensity by the destabilizing effect of streamline curvature, while along the windward face of the hill the opposite signs of the shear strains suppress turbulence by stabilizing curvature effects. The distribution of the turbulent kinetic energy shows maximum values in the reattachment zone, which are similar to the distribution of Reynolds normal and shear stresses.

The results depicted in Figures 4–7 show that maximum values of the normal and shear stresses as well as the turbulent kinetic energy occur in the separating shear layer upstream of reattachment. As expected, the distribution of Reynolds normal stresses in local flow coordinates does not identify any change in sign and exhibits maximum values in the reattachment zone. Following the analysis of Chandrsuda and Bradshaw [33] and Wood and Bradshaw [34], the effect of the shear strain along the streamline direction may be exerted non-locally via the splitting of large eddies at reattachment. This is more likely to cause the observed decrease in Reynolds stresses than the alternative mechanism of alternate downstream and upstream deflection of large eddies at reattachment. The processes of turbulent mixing over most of the flow regime may be described as a response to changes in the mean rates of strain, with the turbulence 'memory' determining how much of the upwind flow is reflected in the measured stresses.

Two aspects of the present flows are of prime practical significance for the reason mentioned above. First, the extent and strength of the recirculation zones established in the leeside of the obstacles, because when separation occurs, for example, in atmospheric flows, it will change the wind field not only in the separation region itself but over the entire hill, so that defining its limits becomes a prerequisite of establishing the overall flow field. Second, the mean velocity speed-up on the hill top holds obvious interest both for wind power engineers and for those interested in predicting wind loading on building and structures, and many investigations of hill flows are aimed at just quantifying this features.

The present computational results suggest that the mean velocities obtained by both IPM and TCL agree reasonably well with the experimental data. However for IPM, there are large discrepancies in prediction for the turbulent stresses in the wake region. In contrast the TCL model provides much improvement for turbulent stresses particularly in the wake region.

4.2. Comparing with other turbulent models

We shall now compare the performance of the IPM and TCL models with two recently developed low-Reynolds number k–ε turbulent models used to calculate the flow field over the same two-dimensional model hill [22,35].

In the low-Reynolds number k–ε model of Goldberg and Apsley, the eddy viscosity $v_t = c_\mu f_\mu k^2/\varepsilon$ is based on the following transport equation:

$$\frac{\mathrm{D}\rho k}{\mathrm{D}t} = \frac{\partial}{\partial x_j}\left[\left(\mu + \frac{\mu_t}{\sigma_k}\right)\frac{\partial k}{\partial x_j}\right] + P - \rho\varepsilon \tag{4.1}$$

$$\frac{\mathrm{D}\rho\varepsilon}{\mathrm{D}t} = \frac{\partial}{\partial x_j}\left[\left(\mu + \frac{\mu_t}{\sigma_\varepsilon}\right)\frac{\partial \varepsilon}{\partial x_j}\right] + (c_{\varepsilon 1}P - c_{\varepsilon 2}\rho\varepsilon + E)T_t^{-1} \tag{4.2}$$

where the time scale realizability is maintained by using

$$T_t = (k/\varepsilon)\max(1, \zeta^{-1}), \quad \zeta = \sqrt{Re_t/c_\tau}$$

This imposes the Kolmogorov scale $\sqrt{v/\varepsilon}$ on the source and sink terms of Equation (4.2) for $Re_\mathrm{t} \ll 1$. The effect of the additional source term

$$E = \frac{2A_k c_{\varepsilon 2}}{c_\tau A_\mu}\mu f_\mu S^2\, \mathrm{e}^{-A_f\sqrt{\varepsilon_k/vS}}$$

is to cancel the non-zero destruction term $c_{\varepsilon 2}\rho\varepsilon$ in the immediate vicinity of walls, where $S = \sqrt{2S_{ij}S_{ij}}$, $S_{ij} = \partial U_i/\partial x_j + \partial U_j/\partial x_i$ and the total kinetic energy $\varepsilon_k = \sqrt{U_i U_i/2 + k}$. The near-wall damping function forces the relation $v_t \sim \overline{v^2}T_t$ through

$$f_\mu = \frac{1 - \mathrm{e}^{-A_\mu Re_\mathrm{t}}}{1 - \mathrm{e}^{Re_\mathrm{t}}}\max(1, \zeta^{-1})$$

The model coefficients are tabulated in Table III.

Figure 8 shows the comparison of IPM and TCL with the above models at the approximate reattachment point $x/H = 4.286$. The prediction shows that the TCL model slightly overestimates the mean horizontal velocity at the height of $y/H \approx 1.5$ (Figure 8(a)) but gives a better estimation for the Reynolds shear stress compared with other models (Figure 8(b)). Note incidentally that the TCL model still underestimates the turbulent shear stress when compared with experimental data. Therefore, is seems that there is still a need for improving the TCL

Table III. The coefficients used by Goldberg and Apsley [22].

c_μ	$c_{\varepsilon 1}$	$c_{\varepsilon 2}$	σ_k	σ_ε	A_μ	A_f	A_k	c_τ
0.09	1.44	1.92	1.0	1.3	0.01	0.214	0.05	$\sqrt{2}$

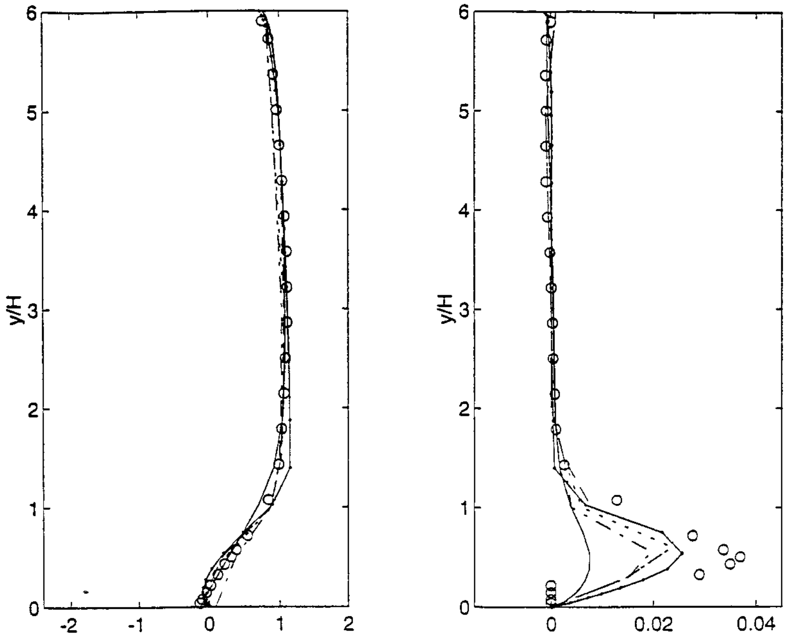

(a) (b)

Figure 8. (a) Non-dimensional mean velocity profiles U/U_0 and (b) non-dimensional turbulent shear stress profiles $-\overline{uv}/U_0^2$ at the location $x/h = 4.286$; ---, TCL model; —, IPM model; · · · Lien and Leschziner model; - - -, Goldberg and Apsley model; ○, experimental data of Almeida *et al.* [5].

model further, in particular for the flow behind a hill where substantial turbulent mixing takes place.

5. CONCLUSION

In this paper computational results for turbulent flow over a large-amplitude hill mounted in a water tunnel at $Re = 6 \times 10^4$ is reported and is compared with laboratory measurements of Almeida *et al.* [5]. The calculations performed here, just like the experiment of Almeida *et al.* [5], correspond to a neutrally stratified flow regime characterized by a ratio of the upstream shear layer thickness to the height of the hill, which is less than unity. The aim of this investigation was to establish the effect of streamline curvature on the nature of the turbulent flow over the hill and to develop a realizable turbulence model in order to allow extrapolation to more practical situations for the purpose of improving our knowledge of complex flow situations of engineering interest.

The outcome of calculations shows that a flow structure with a thin boundary layer is established on the rising surface of the hill and accelerates up to the crest. The separation point occurs on the downstream surface of the hill and extends up to $x/h = 4.821$. The curvature of the flow imposes mean velocity effects on the turbulent flow resulting in the establishment of a zone of high-intensity velocity fluctuations along the shear layer downstream of the top of the hill, which are rapidly suppressed with the approach of the reattachment zone. The results suggest that the upper half of the shear layer interacts with the outer flow in a way similar to that of a plane shear flow.

The results also show that the turbulent kinetic energy increases with the distance from the top of the hill up to the reattachment point and then decreases significantly due to the upward tilting of the flow at the upstream face of the hill. This is because downstream of the top of the hill the overall effect of positive shear strains increases turbulence intensity by the destabilizing effect of streamline curvature, while along the windward face of the hill the opposite sign of the shear strains suppress turbulence by stabilizing curvature effects.

To accurately reproduce the behaviour of the turbulent stresses, it is necessary to consider the differing responses of the component variances to straining by the mean flow, to changes in the dissipation rate, to the effort of turbulence 'memory' and to sudden changes in turbulence length scales as the wake flow is approached. In this respect, the TCL model adopted here proved to be more superior because, unlike the IPM model, it is not strongly biased toward the near-equilibrium situations and avoids the use of gradient diffusion model for triple correlations. Also in the TCL model, the geometry-specific quantities, such as the wall-normal vector or wall distance, are replaced by invariant dimensionless gradient indicators in order to correct for strong inhomogeneity in the wall vicinity and the damping of the fluctuating velocity component normal to the wall. Furthermore, the model uses a new decomposition for the fluctuating pressure terms, and captures the diverse behaviour of the different components of the stress dissipation near the wall.

In conclusion, the low-Reynolds number TCL model adopted here provides a much better tool for predicting the flow field and turbulent stresses for flows over complex geometries as was demonstrated in the present study. It is also shown here that the level of turbulent stresses predicted by the TCL model agrees much better with the laboratory measurements for separated flow of two-dimensional model hill than that predicted by the conventional low-Reynolds number IPM model. In particular, better agreement between the TCL model and the measurements for turbulent stresses is obtained in the far-field recovery region. However, in the separation region, the TCL model still underestimates the level of turbulence stresses. This point needs to be addressed and clearly requires further study in order to improve the present TCL model.

REFERENCES

1. Mueller A, Gyr A. Visualization of the mixing layer behind dunes. In *Proceedings of Euromech 165. The Mechanics of Sediment Transport*. A.A. Balkema: Rotterdam, 1982; 41–45.
2. Hunt JCR, Snyder WH. Experiments on stably and neutrally stratified flow over a model three-dimensional hill. *Journal of Fluid Mechanics* 1980; **96**: 671–704.
3. Dumas R, Fulachier L. *Proceedings of the IUTAM Symposium on the Structure of Complex Turbulent Shear Flows*, Marseilles, France, 1982.
4. Durão DFG, Heitor MV, Pereira JCF. A laser anemometry study of separated flow over a model three-dimensional hill. In *Applications of Laser Anemometry to Fluid Mechanics*, Adrian *et al.* (eds). Springer: New York, 1989; 93–118.

5. Almeida GP, Durão DFG, Heitor MV. Wake flows behind two-dimensional model hills. *Experimental Thermal and Fluid Science* 1993; **7**: 87–101.
6. Deaves DM. Computations of wind flow over two-dimensional hills and embankments. *Journal of Wind Engineering and Industrial Aerodynamics* 1980; **6**: 89–111.
7. Mason PJ, King JC. Atmospheric flow over a succession of nearly two-dimensional ridges and valleys. *Quarterly Journal of the Royal Meteorological Society* 1984; **110**: 821–845.
8. Sajjadi SG, Hunt JCR, Wong H. Homogeneous turbulence approaching a wavy surface. In *Proceedings of Wind-Over-Wave Couplings*, Sajjadi SG, Thomas NH, Hunt JCR (eds). Oxford University Press: Oxford, 1999.
9. Launder BE, Reece CG, Rodi W. Progress in the development of a Reynolds-stress turbulence closure. *Journal of Fluid Mechanics* 1975; **68**(3): 537–566.
10. Lumley JL. Computational modelling of turbulent flows. *Advances in Applied Mechanics* 1978; **18**: 123.
11. Gibson MM, Launder BE. Ground effects on pressure fluctuations in the atmospheric boundary layer. *Journal of Fluid Mechanics* 1978; **86**(3): 191–511.
12. Reynolds WC. Physical and analytic foundations, concept and new directions in turbulence modelling and simulation. In *Turbulence Models and their Applications*, vol. 2. Eyrolles: Paris, 1984.
13. Fu S, Launder BE, Tselepidakis DP. Accommodating the effects of high strain rates in modelling the pressure–strain correlation. Report No. TFD/87/5, Mechanical Engineering Department, UMIST, 1987.
14. Lee MJ. A contribution toward rational modelling o the pressure–strain-rate correlation. *Physics Fluids A* 1990; **2**(4): 630–633.
15. Shih TH, Lumley JL. Modelling of pressure correlation terms in Reynolds stress and scalar flux equations. Report No. FDA-85-3, Cornell University, Ithaca, New York, 1985.
16. Craft TJ. Computaions of separating and reattaching flow using a low-Reynolds-number second-moment closure. In *Proceedings of the 11th Turbulent Shear Flows Symposium*, Grenoble, 8–11 September 1997.
17. Murakami S, Kato S, Kondo Y. Examining k–ϵ EVM by means of ASM for 3-D horizontal buoyant jet in enclosed space. In *Engineering Turbulence Modelling and Experiments*, Rodi W, Ganić EN (eds). Elsevier: Amsterdam, 1990.
18. Craft TJ, Launder BE. New wall-reflection model applied to the turbulent impinging jet. *AIAA Journal* 1992; **32**(12): 2970–2972.
19. Craft TJ, Launder BE. A Reynolds-stress closure designed for complex geometries. *International Journal for Heat and Fluid Flow* 1996; **17**: 245–254.
20. Bonnin JC, Buchal T, Rodi W. ERCOFTAC Workshop on Data Bases and Testing of Calculation Methods for Turbulent Flows. In *ERCOFTAC Bulletin*, 1995; 48–54.
21. Lien FS. A simple low-*Re* cubic eddy-viscosity model. UMIST 7th Biennial Colloquium on CFD, Paper 2.2, 1996.
22. Goldberg U, Apsley D. A realisable wall-distance-free two-equation eddy-viscosity model. UMIST 7th Biennial Colloquium on CFD, paper 2.1, 1996.
23. Rotta J. Statistische Theorie nichthomogener Turbulenz I. *Zeitschrift Fur Physik* 1951; **129**: 547–572.
24. Hanjalic K, Launder BE. A Reynolds stress model of turbulence and its application to thin shear flows. *Journal of Fluid Mechanics* 1972; **52**: 609–638.
25. Launder BE, Tselepidakis DP. Contribution to the modelling of near-wall turbulence. In *Turbulent Shear Flows*, vol. 8, Durst F *et al.* (eds). Springer: New York, 1993; 81–96.
26. Kim J, Moin P, Moser R. Turbulence statistics in fully developed channel flow at low Reynolds number. *Journal of Fluid Mechanics* 1987; **177**: 133.
27. Millionshtchikov MD. On the theory of homogeneous isotropic turbulence. *Compte rendu de l'Academie des Sciences de l'U.R.S.S.* 1941; **32**: 615.
28. Leonard BP. A stable and accurate convective modelling procedure based on quadratic upstream interpolation. *Computer Methods in Applied Mechanics and Engineering* 1979; **19**: 59–98.
29. van Leer B. Towards the ultimate conservative difference scheme V, a second-order sequel to Godunov's method. *Journal of Computational Physics* 1979; **32**: 101.
30. Sajjadi SG, Aldridge JN. Prediction of turbulent flow over asymmetrical bed forms. *Journal of Applied Mathematical Modelling* 1995; **19**(3): 139.
31. Sajjadi SG, Waywell MN. A stable algorithm for Reynolds stress turbulence modelling with application to rectilinear and circular tidal flows. *International Journal for Numerical Methods in Fluids* 1998; **26**: 251.
32. Buckles JJ, Hanratty TJ, Adrian RJ. Turbulent flow over large-amplitude wavy surfaces. *Journal of Fluid Mechanics* 1984; **140**: 27–44.
33. Chandrsuda C, Bradshaw P. Turbulence structure of a reattaching mixing layer. *Journal of Fluid Mechanics* 1981; **110**: 171–194.

34. Wood DH, Bradshaw P. A turbulent mixing layer constrained by a solid surface. Part 2. Measurements in the wall-bounded flow. *Journal of Fluid Mechanics* 1984; **139**: 347–362.
35. Lien FS, Leschziner MA. A general non-orthogonal collocated finite-volume algorithm for turbulent flow at all speeds, incorporating second-moment turbulence-transport closure. Part 1: computational implementation. *Computer Methods in Applied Mechanics and Engineering* 1994; **114**: 123.